Effect of Rheocasting on Corrosion of AM50 Mg Alloy

Citation for the original published paper (version of record):
Esmaily, M., Mortazavi Seyedeh, N., Shahabi Navid, M. et al (2015). Effect of Rheocasting on Corrosion of AM50 Mg Alloy. Journal of the Electrochemical Society, 162(3): C85-C95. http://dx.doi.org/10.1149/2.0331503jes

OPEN ACCESS

Effect of Rheocasting on Corrosion of AM50 Mg Alloy

Effect of Rheocasting on Corrosion of AM50 Mg Alloy

M. Esmaily,[a,*,z] N. Mortazavi,[b] M. Shahabi-Navid,[a,*] J. E. Svensson,[a,] M. Halvarsson,[b] L. Nyborg,[c] M. Wessén,[d] A. E. W. Jarfors,[d] and L. G. Johansson[a]**

[a]*Department of Chemical and Biological Engineering, Chalmers University of Technology, SE-412 96 Göteborg, Sweden*
[b]*Department of Applied Physics, Chalmers University of Technology, SE-412 96 Göteborg, Sweden*
[c]*Department of Materials & Manufacturing Technology, Chalmers University of Technology, SE-412 96 Göteborg, Sweden*
[d]*Department of Materials and Manufacturing - Casting, Jönköping University, SE-551 11 Jönköping, Sweden*

The corrosion behavior of magnesium-aluminum (Mg-Al) alloy AM50 produced by a rheocasting (RC) technique was examined in the presence and absence of CO_2 at three temperatures −4, 4 and 22°C. The slurry preparation in the RC material was performed with the newly developed RheoMetal process. For reference, 99.97% Mg was included in the corrosion exposures. The influence of the microstructure on the atmospheric corrosion of alloy AM50 produced by RC and high pressure die casting (HPDC) was investigated. The RC AM50 alloy showed better corrosion resistance than HPDC AM50 in all the exposure environments studied. For both materials, there was a strong positive correlation between temperature and the atmospheric corrosion rate. The superior atmospheric corrosion behavior of RC AM50 compared to HPDC AM50 is carefully discussed in relation to differences in the as-cast microstructure. This study demonstrates that producing the alloy AM50 by this type of RC technique opens the door to Mg-Al alloys as a promising candidate for various applications where corrosion resistance is of importance.
 [DOI: 10.1149/2.0331503jes]

Manuscript submitted November 18, 2014; revised manuscript received December 9, 2014. Published December 16, 2014.

Magnesium-aluminum (Mg-Al) alloys are being employed in the automotive and many other engineering sectors owing to their high specific strength, high specific stiffness, good castability and recycleability, excellent machinability and abundant resources.[1–4] Thus, they offer several advantages from the weight reduction and energy savings points of view. However, the more widespread use of MgAl alloys is limited by their low corrosion resistance and poor high temperature mechanical properties.[5–8] The corrosion properties of Mg-Al alloys have therefore attracted scientific attention. Currently, the majority of Mg-Al cast components are produced by conventional high-pressure die casting (HPDC). One of the main problems of thick-walled Mg-Al components made by HPDC is the relatively high fraction of porosity caused by the turbulent die filling. The pores function as local stress concentrators and can severely degrade mechanical properties and porosity also interferes with the heat-treatment of cast components.[9,10]

Semi-solid casting is an alternative manufacturing technique that can be used to produce castings with a high level of complexity. In this process, a semi solid slurry is used, which shows non-turbulent or thixotropic flow behavior. Semi-solid cast alloys offer some advantages over their HPDC counterparts. For instance, porosity is lower due to laminar mould-filling and lower solidification shrinkage.[11,12] Thixo-forming and rheocasting (RC) are the main semi-solid manufacturing processes. In thixo-forming, a near-net shape forming process is achieved using a partially melted, non-dendritic alloy slug.[12] In contrast, RC involves preparation of a semi-solid slurry from the liquid alloy by cooling. In the RheoMetal process (also called the RSF process or the Rapid S process) cooling is performed by using an enthalpy exchange material (EEM) attached to a stirrer.[13] Thus, the metal is cooled internally which eliminates the need for external heat flow control, thereby creating a robust process where large amounts of high quality slurry can be produced in a short time. After slurry preparation the metal is used in a casting operation; typically similar to traditional HPDC.[13] The RC method has shown great potential for overcoming some of the inherent problems in other casting methods. In order to implement the RC process to fabricate Mg alloys for various applications, the properties of the as cast materials have to be carefully characterized and, especially, the corrosion behavior has to be investigated.

The effect of microstructure on the corrosion behavior of Mg alloys produced by different casting techniques has been reported by several workers.[14–20] It is kwon that the atmospheric corrosion behavior of Mg-Al alloys is strongly influenced by microstructure, especially the distribution and composition of the main microstructural constituents.[21–23] The β phase is reported to be cathodic in comparison to α-Mg, the two phases forming micro-galvanic corrosion cells on the alloy surface.[24,25] Besides accelerating corrosion by acting as a cathode, the β phase can also function as a corrosion barrier in Mg-Al alloys.[15,24] The cathodic activity of the η phase has also been reported by several authors.[26,27]

The corrosion behavior of Mg-Al alloys produced by different casting technologies has also been studied.[17,28] For example, Asmussen et al.[17] studied the corrosion behavior of alloy AM50 produced by sand, graphite and die castings in 1.6 wt% NaCl solution and reported that the alloy produced by the die casting shows better corrosion resistance compared to that of the alloy produced by sand and graphite castings. Despite the large amount of literature about corrosion of Mg alloys, the corrosion behavior of semi-solid cast Mg-Al alloys in comparison to the same alloy produced by conventional HPDC technique is largely unexplored. In automotive applications, quite corrosive conditions are encountered in connection to the use of deicing salt in the wintertime. Therefore, it becomes interesting to investigate the atmospheric corrosion behavior of Mg alloys in the presence of NaCl at temperatures close to or below 0°C. There are very few studies on the effect of temperature on atmospheric corrosion of Mg alloys. In a preliminary study, the authors investigated the effect of temperature on NaCl-induced atmospheric corrosion behavior of HPDC AM50 in the presence and absence of 400 ppm CO_2.[29] The NaCl-induced corrosion of the alloy was found to exhibit a strong positive temperature dependency. Chen et al. [30] also reported on a positive correlation between corrosion attack and temperature for the initial stages (2h) of atmospheric corrosion of the Mg-Al alloy AZ91 between 2°C and 8°C. However, the atmospheric corrosion behavior of semi-solid Mg-Al alloy at minus temperatures has not been reported. Thus, the present paper investigates the corrosion behavior of the Mg-Al alloy AM50 at different atmospheric environment for the two casting methods: RC and HPDC. The differences in atmospheric corrosion behavior of the materials are discussed in terms of the microstructure.

*Electrochemical Society Student Member.
**Electrochemical Society Active Member.
zE-mail: mohsen.esmaily@chalmers.se

Experimental

Test alloys.— The test materials were HPDC and RC AM50. 99.97% Mg was used as a reference material. The HPDC AM50 was supplied from a commercial manufacturer (Finnveden Metal Structures AB). The semi-solid AM50 castings, supplied by Jönköping University, were produced by a relatively new slurry preparation process called as the RheoMetal process, which is a recently developed industrial-scale RC process.[13] The semi-solid castings were using a vertical casting machine with a locking force of 50 tons and capable of casting parts with a maximum projected area of 250 cm^2. Some of the processing parameters adopted to produce the RC parts using the RheoMetal process are as follows:

- Amount of EEM: 4% of the total slurry weight
- Superheat temperature of the melt: 50 ± 5°C
- Die temperature: varied between 100–200°C
- Slurry temperature: 621°C
- Cycle time for each casting: 60s
- Slurry temperature: 621°C

The chemical compositions of the unalloyed Mg as well as RC and HPDC materials were analyzed by optical mass spectroscopy and are listed in Table I. As-received materials were cut to produce 14 × 14 × 3 mm^3 corrosion samples with a surface area of 5.56 cm^2. For both microstructural characterization and corrosion experiments, the samples were first ground by SiC grit papers from P1000 to P4000 mesh. Polishing was performed with cloth discs and diamond paste in the range of 1–3 μm, following by a fine polishing step by colloidal silica.

Microstructure characterization.— An area of 1.47 mm^2 was selected from longitudinal and cross-section of the RC and HPDC AM50 for the microstructural quantification by image processing. To conveniently compare the microstructure of the alloy produced by the two casting technologies, care was taken that the investigated samples were the same with respect to bar thickness (20 mm) and the distance from the surface of the casting (1.5 mm). A solution of Nital (5 ml HNO_3 + 95 ml ethanol) was used as an etching reagent to reveal the constituents and general microstructure of the alloy.

The constituents were examined by both optical microscope (OM) and a FEI Quanta 200 environmental scanning electron microscopy (ESEM) equipped with Oxford Link energy dispersive X-ray (EDX) microanalysis hardware. Quantitative metallography was performed with the image analysis software ImageJ and Image Pro-Plus. The strategy to quantify all the microstructural features such as fraction of pore, inter-dendritic regions, intermetallic phase particles, and aspect ratio of α-Mg grains is provided in.[31] The aspect ratio was defined as $F = 4\ \pi A/P^2$, where A is the area and P is the peripheral length of a grain.

Atmospheric corrosion exposures.— Corrosion experiments on 99.97% Mg and the RC and HPDC alloys were performed at three different temperatures, 22, 4, and −4 ± 0.3°C, both in the presence and absence of 400 ppm CO_2. The experimental set-up for the exposures at ambient and below ambient temperatures with and without CO_2 is described elsewhere.[29] The exposure apparatus was entirely made in glass and Teflon. The samples were suspended by a nylon string in individual exposure chambers. The gas flow was 1000 ml/min corresponding to an average flow velocity of 1 mm/s. Relative humidity (RH) was regulated to be 95 ± 0.2% by mixing measured amounts of dry air and 100% RH air. CO_2 was added from a cylinder to give a constant concentration of 400 ± 20 ppm. A new corrosion system was designed and used in order to perform corrosion experiment at sub-zero temperature,.[29] Ethylene glycol was used as coolant. In addition, two internal humidifiers were placed inside the liquid of the pool to decrease the dew point of the humidified air to −4°C.

The corrosion exposures in the absence of CO_2 were carried out in hermetically closed desiccators (as corrosion reactors) with a volume of 3 dm^3. The 95% humid air was achieved by equilibrating with 500 ml potassium hydroxide solution (KOH (aq)) in a container placed inside the desiccator. The water vapor partial pressure over KOH (aq) was calculated by the following equation;[32]

$$\log p_{w\,(KOH)} = -0.01m - 0.001m^2 + 2.2 \times 10^{-5}m^3 + (1 - 0.001m + 5.6 \times 10^{-4}m^2 - 7.8 \times 10^{-6}m^3) \times (35.4 - 3343.9/T - 10.9 \log T + 0.01\,T)(\text{bar}) \quad [1]$$

where P_w is the equilibrium partial pressure of water vapor over the aqueous solution, m is the molality and T is the experiment temperature. In addition to regulating the relative humidity to the desired value, i.e. 95% RH, the KOH (aq) solution also functions as a CO_2 absorbent.

Prior to the exposures, the samples were contaminated with two different amounts of salt, 14 and 70 μg/cm^2, using a solution of 20 ml distilled water, 80 ml ethanol and 1 g NaCl. A relatively long-exposure time of 840 h was selected to investigate the corrosion resistance of the alloys. Duplicate and triplicate samples were used for each condition to increase the reliability of the data.

Methods of analysis.—Gravimetric measurements.— To monitor the atmospheric corrosion process the test coupons were removed from corrosion reactors during the exposures for weighing with regular intervals except for the CO_2-free exposures. Therefore, much of the water contained in the NaCl electrolyte remains during weighing and the corresponding mass gains are accordingly called wet mass gains. At the conclusion of an exposure, after measuring the wet mass, the samples were stored for 24 hours at room temperature over a desiccant so that the loosely bound water was removed. The specimens were weighed again and the corresponding mass gains are termed dry mass gains. The quantity of corrosion product was determined via leaching and pickling processes of the corroded specimens using agitating ultrasonic bath at room temperature. The water soluble corrosion products and unreacted NaCl were first removed by a leaching process. To do this, the samples were first immersed in Milli-Q water (ultrapure water) in two steps; 30 and 60 s at 25°C. Subsequently, the corroded samples were pickled several times in a chromate solution of 20% chromium trioxide (CrO_3) for 15 s followed by several periods of 30 s. Metal loss values were obtained by the equation $M_{loss} = (M_O) - (M_P)$, where M_{loss} is metal loss, M_O is mass before exposure and salt and M_P is mass after final stage of pickling.

Analytical scanning electron microscope (SEM/EDX).—The morphology of the corrosion products was examined by an FEI Quanta 200 environmental scanning electron microscopy (ESEM) with a Schottky field emission gun (FEG). The instrument was equipped with energy dispersive X-ray detector (EDX) system. SEM/EDX was used for local chemical analysis as well as elemental mapping of the corroded metal surfaces and the milled cross sections. Nearest neighbor distance (NND), which also called as closest point search, of the

Table I. Composition of the test materials (% by weight).

	Mg	Al	Mn	Si	Zn	Fe	Cu	Ni	Be
RC AM50	Balance	5.6	0.26	0.012	0.007	0.001	0.0004	0.0003	0.0004
HPDC AM50	Balance	5.9	0.25	0.014	0.009	0.001	0.0009	0.0006	0.0002
99.97% Mg	Balance	0.003	0.0023	0.003	0.0050	0.0018	0.0003	0.0002	-

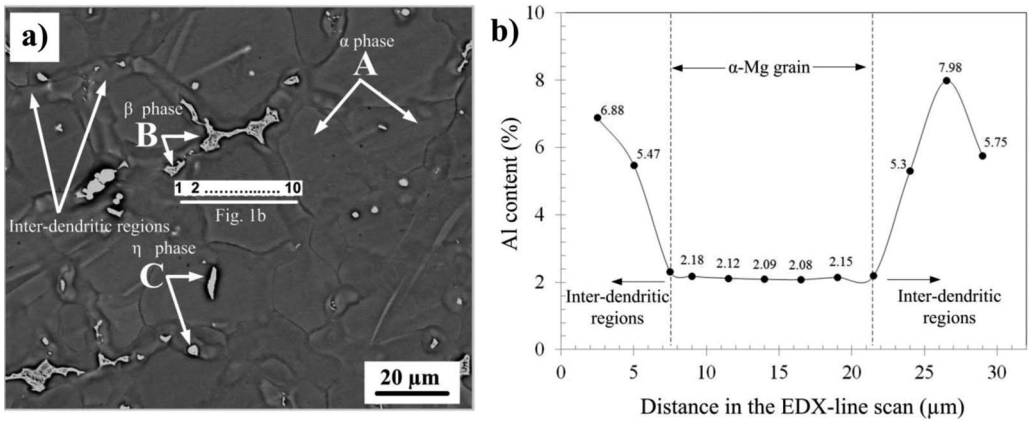

Figure 1. (a) Typical SEM micrographs of AM50 alloy, showing an overview of the microstructure, (b) a line scan that shows the Al concentration in a α-Mg dendrite and in the surrounding regions. Note: EDX point analysis of A, B and C are presented in Table II.

corrosion crusts formed on the corroded surfaces of the RC and HPDC materials was calculated on the SEM images to describe the arrangement of corrosion products formed on alloy surfaces in a quantitative manner. The NND is a mathematical function that attempts to optimize a problem by finding closest (or most similar) points. The NND is a probability density function such that P(r) dr is the probability of finding the nearest neighbor of a particle with the same characteristics in the distance range r to (r+ dr). More details are provided in.[31,33,34]

Optical profilometry.—The evaluation of the corrosion pits formed on the materials as well as the surface damage were carried out using an interference microscope (RST plus) from WYKO using vertical scanning-interferometry (VSI) mode. A 5× objective (producing a 1.3 × 0.9 mm^2 field of view) was used for this study. The data were then converted for obtaining 3 dimensional (3D) surface topography measurements.

Results

Microstructure characterization.— Figure 1 shows the typical solidification microstructure of a HPDC AM50 alloy, which was characterized by primary α-Mg dendrites, inter-dendritic areas and casting defects, e.g., pores. The inter-dendritic regions are decorated by intermetallics, i.e., β ($Mg_{17}Al_{12}$) and η ($Al_8Mn_{5-x}Fe_x$) phases. The elemental compositions of different macro- and micro-constituents are listed in Table II. An understanding of the differences in the atmospheric corrosion behavior of materials produced by the two casting technologies required a careful quantification of the as-cast microstructures, including the Al concentration, the size and morphology of the α-Mg dendrites and the volume fraction and distribution of intermetallic particles.

Aluminum concentration in α-Mg dendrites.—Figure 1 also shows a typical EDX profile across a typical α-Mg dendrite (indicated in the SEM image), exhibiting an average Al concentration of about 2.1 wt%. The Al concentration reached to about 8 wt% in the inter-dendritic regions containing a eutectic mix of α and β phases, see the line scan analysis in Fig. 1a. Line-scan analyses were carried out on 60 primary α-Mg grains in both RC and HPDC AM50, with grain sizes in the range 20 to 30 µm. The results showed that there is no significant Al gradient within the α-Mg grains in the two materials. The average Al concentration in the α-Mg grains was 1.9 ± 0.25 wt% in the HPDC material while the corresponding value for the RC alloy was slightly less with a value of 1.8 ± 0.15 wt%.

Characterization of α-Mg dendrites and porosity.—Table III lists quantitative information on the size and area fraction of the primary α-Mg grains and the inter-dendritic regions as well as the area fraction of pores. Both the area fraction of primary α-Mg grains and the average grain size were larger in the RC material compared to the HPDC material, indicating the formation of a coarser microstructure in the RC AM50. Correspondingly, the area fraction of the inter-dendritic regions was lower for RC AM50 than for HPDC AM50. In the HPDC AM50 alloy, the dendritic structure was more pronounced and α-Mg grains were larger for regions closer to the center of casting. The dendritic structure was much less pronounced in the RC material, the primary α-Mg grains showed a higher aspect ratio, i.e. being more globular, see Table. II. While both materials exhibited defect bands more or less parallel to the cast skin with a high fraction of pores, the percentage of porosity was three times greater in the HPDC material compared to the RC AM50 alloy, see Table III. In the RC material, the pores were mainly associated with the β phase and the inter-dendritic areas with sizes in the range 10–80 µm. Macro-porosities corresponding to gas pores in the size range 50–250 µm were more frequent in the HPDC material.

Characterization of intermetallic particles.—Figure 2 shows bright-field and corresponding dark-field OM images of etched as-cast microstructures of HPDC and RC AM50. Although β and η intermetallic particles cannot be distinguished in the OM dark-field image, the area fraction of η particles was not more than 0.35 and 0.4% in RC and HPDC AM50, respectively. Thus, the OM dark-field images could be used as a standard qualitative method for characterizing the distribution, size and morphology of the β phase particles in both materials.

The β phase was observed in the inter-dendritic regions, appearing as dispersed fine particles in the HPDC alloy and as coarser and more continuous particles in the RC alloy. In contrast, η phase ($Al_8Mn_5(Fe)$) was observed both in the inter-dendritic regions and within the α-Mg grains, see the BSE SEM micrograph in Fig. 1. According to the quantitative image analyses, the β phase fraction was about three times higher in the RC material than in the HPDC material, see Table III. The higher fraction of β phase in the RC material

Table II. Elementary composition of main phases (wt%) related to the points designated in Fig. 1.

Point	Mg	Al	Mn	Fe
A (α-Mg)	93.4 ± 0.9	1.9 ± 0.2	-	-
B (β eutectic $Mg_{17}Al_{12}$)	63.2 ± 1.5	33.5 ± 1.8	-	-
C (η phase $Al_8Mn_5(Fe)$)	34.1 ± 0.4	30.3 ± 1.1	34.7 ± 2.3	0.9 ± 0.08

Table III. The area fraction and size of different microstructural features in the RC and HPDC AM50.

	Primary α-Mg area fraction (%)	Primary α-Mg size (μm)	Primary α-Mg aspect ratio	Inter-dendritic region area fraction (%)	β-phase area fraction (%)	Porosity (%)
RC AM50	80.4 ± 5	35 ± 9	0.75	12.5 ± 4	5.9 ± 0.9	1.2 ± 0.5
HPDC AM50	68 ± 3	26 ± 4	0.42	26.4 ± 3	1.9 ± 0.4	3.7 ± 0.7

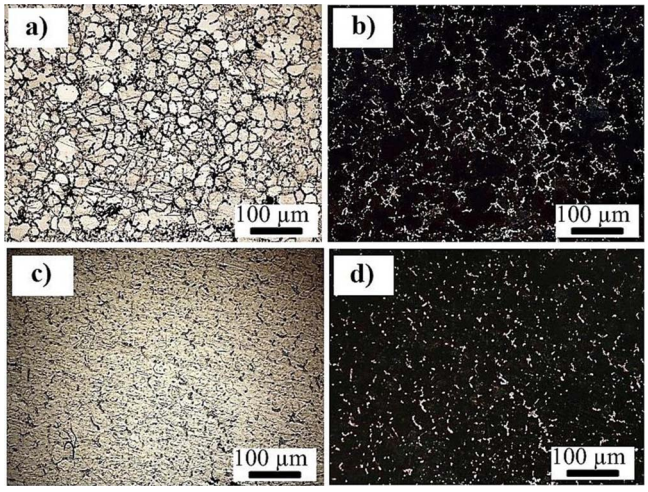

Figure 2. Bright-field and corresponding dark-field OM images showing the different distribution and size of second phase particles in; (a and b) RC AM50, (c and d) HPDC AM50.

compared to the HPDC material can be qualitatively seen in Fig. 2b and 2d. While the fraction of β phase was found to be 3 times higher in the RC material than in HPDC material, it is cautioned that the measured fractions of β phase in this study are obtained from one cross section of the castings and may not be representative of the entire RC and HPDC materials.

The distribution of intermetallics was much less uniform in the HPDC material than RC material, compare Figs. 3a and 3b with Fig. 3c. Thus, the HPDC AM50 exhibited some regions (only one in the entire projected area) with a very high fraction of intermetallics, see Fig. 3a, while the rest of the material exhibited a relatively low fraction of intermetallic particles, see Fig. 3b. In contrast, no regions with a strong accumulation of intermetallic particles were detected in the RC material. It is worth mentioning that the regions with a local accumulation of intermetallic phases (see Fig. 3a) were excluded from the quantitative analyses as these areas were not representative of the HPDC microstructure. The electrochemical response of such areas with high fraction of β phase will be a topic of future study. Fig. 3 shows the size distribution and number of intermetallics for both alloys. In both cases the examined area was 1.47 mm^2. In accordance with the OM images (Fig. 2) that indicate a more continuous and network-like morphology for the β particles in RC AM50 compared to the HPDC material, the statistical analysis indicates the RC material contains larger β phase particles. It may be noted that the total number of intermetallic particles detected was 783 and 612 for RC and HPDC AM50, respectively.

Atmospheric corrosion behavior of RC and HPDC AM50.— Gravimetric data analysis.— Table IV and Fig. 4 present mass gains, metal losses and corrosion rates for the two materials exposed at −4, 4 and 22°C with different amounts of added NaCl. The reproducibility of the data is presented in Table IV. The influences of NaCl, temperature

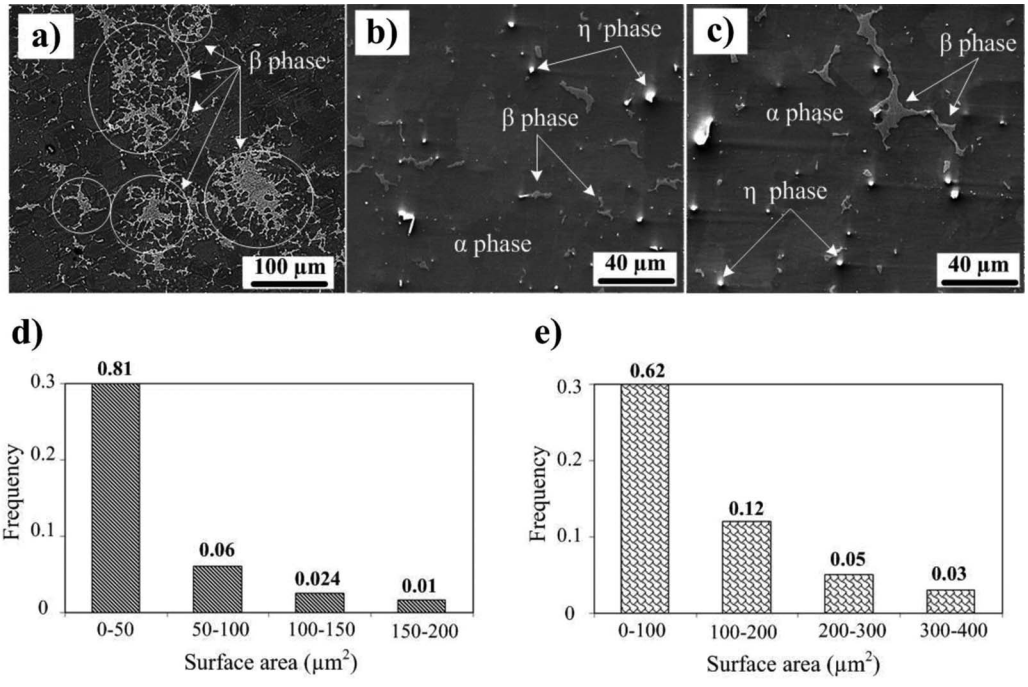

Figure 3. Solidification microstructures of alloy AM50, (a and b) HPDC AM50, showing the strong accumulation of intemetallics in the HPDC material, (c) RC AM50. The size distribution of β phase particles in the (d) HPDC alloys and (e) RC alloy. The total number of intermetallics for HPDC and RC alloys was 783 and 612, respectively, in the studied regions.

Table IV. Average dry mass gains, metal losses, and corrosion rates for HPDC and RC AM50 after 840 h exposure at different environments.

CO_2	Temp. (°C)	NaCl ($\mu g/cm^2$)	Average dry mass gain (mg/cm^2) RC	Average dry mass gain (mg/cm^2) HPDC	Metal loss (mg/cm^2) RC	Metal loss (mg/cm^2) HPDC	Corrosion rate (μm/year) RC	Corrosion rate (μm/year) HPDC
400 ppm	22	Ref.	0.06*	0.04*	0.03*	0.02*	2**	2**
		14	0.60 ± 0.1	0.74 ± 0.1	0.18 ± 0.09	0.27 ± 0.1	14 ± 0.3	20 ± 0.2
		70	1.59 ± 0.2	2.41 ± 0.1	0.61 ± 0.3	0.99 ± 0.1	46 ± 2.4	72 ± 2
	4	Ref.	0.03*	0.01*	0.01*	0.01	<1**	<1**
		14	0.12*	0.18 ± 0.0	0.05 ± 0.03	0.08*	4**	3 ± 0.4
		70	0.50 ± 0.1	1.31 ± 0.1	0.16 ± 0.04	0.64 ± 0.1	12 ± 0.1	47 ± 2
	−4	Ref.	0.01*	0.01*	<0.01*	0.01*	<1**	<1**
		14	0.07*	0.08*	0.03*	0.04*	2**	3**
		70	0.15*	0.20*	0.06 ± 0.04	0.09*	4**	6 ± 0.2
W/O	22	Ref.	0.03*	0.02*	0.02*	0.01*	2**	2**
		14	1.18 ± 0.1	1.38 ± 0.1	0.74 ± 0.3	0.86 ± 0.2	47 ± 2.3	59 ± 2.5
		70	2.53 ± 0.3	2.76 ± 0.2	1.58 ± 0.2	1.62 ± 0.4	85 ± 1.5	117± 3
	4	Ref.	0.02*	0.01*	0.01*	0.01*	<1**	<1 **
		14	0.41 ± 0.1	0.66 ± 0.2	0.29*	0.47 ± 0.1	22 ± 0.2	34 ±
		70	0.89 ± 0.2	2.03 ± 0.4	0.51 ± 0.1	1.23 ± 0.3	38 ± 1	89 ± 2.9
	−4	Ref.	0.02*	0.03*	0.01*	0.02*	<1**	<1**
		14	0.33 ± 0.1	0.59 ± 0.2	0.23 ± 0.1	0.26 ± 0.1	17 ± 1.2	19 ± 1.1
		70	0.55 ± 0.1	1.26 ± 0.1	0.27 ± 0.2	0.73 ± 0.2	20 ± 2.2	53 ± 2.4

*The scatter for these cases (mass gain and metal loss values) were negligible (<± 0.003 mg/cm^2).
**The scatter for these cases (corrosion rates) were negligible (<± 0.1 μg/year).

and microstructure on the atmospheric corrosion of the investigated alloys are presented separately below.

The influence of NaCl.—In the absence of NaCl, corrosion rates were very small, the highest corrosion rate (2 μm/year) being detected at 22°C. Otherwise the corrosion rates were <1 μm/year. As expected, the mass gains were much greater in the presence of NaCl. Also, increasing the amount of NaCl from 14 to 70 $\mu g/cm^2$ resulted in a large increase in mass gain for both materials.

The influence of CO_2.—In accordance with earlier reports on the inhibitive effect of CO_2 on the atmospheric corrosion of Mg alloys,[35] the present results show that the corrosion is considerably slower in the presence of 400 ppm CO_2 than in the absence of CO_2, irrespective of casting technology and at all three temperatures; see Table IV. For example, at −4°C with 70 $\mu g/cm^2$ added NaCl, the metal loss is 5 and 8 times larger in the CO_2-free exposures compared with the exposures in the presence of 400 ppm CO_2 for RC and HPDC materials, respectively. The strong inhibitive effect of CO_2 is seen in the gravimetric data presented in Table IV.

The influence of temperature.—The mass gain, metal loss and corrosion rate data showed that there is a strong positive correlation between exposure temperature and the rate of atmospheric corrosion of both materials, see Table IV and Fig. 4. A decrease in temperature from 22°C to −4°C resulted in a considerably slower corrosion rate, irrespective of the NaCl amount and the alloy. Thus, from 22° to −4C, the rate of corrosion decreases by a factor of 11 and 12 for RC and HPDC AM50, respectively. In contrast, no clear temperature dependency was observed for 99.97% Mg, see Fig. 4.

Comparing the corrosion behavior of RC and HPDC AM50.—As expected, the corrosion of alloy AM50 produced by both casting techniques is considerably slower than that of 99.97% Mg, independent of the amount of salt, temperature and exposure time, see Fig. 4. The alloy produced by the semi-solid method had a markedly better atmospheric corrosion resistance in the presence of NaCl. For instance, the average metal loss values related to the HPDC material exposed in the presence of 400 ppm CO_2 were 150 to 400% greater than those of the RC material. In contrast, the dry mass gain values in the absence

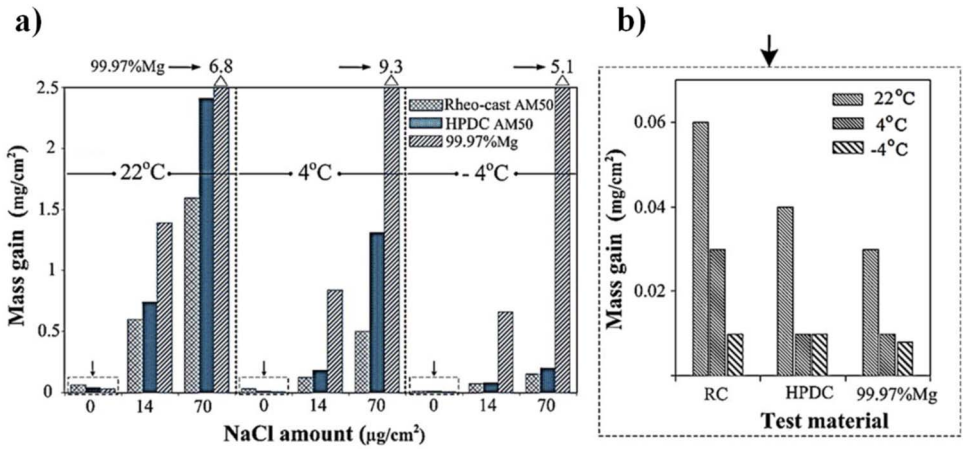

Figure 4. (a) The effect of temperature and the amount of NaCl added on the mass gain of RC, HPDC AM50 and 99.97% Mg in the presence of 400 ppm CO_2, (b) the mass gain data in the absence of NaCl. Note: The scatters are provided in Table IV.

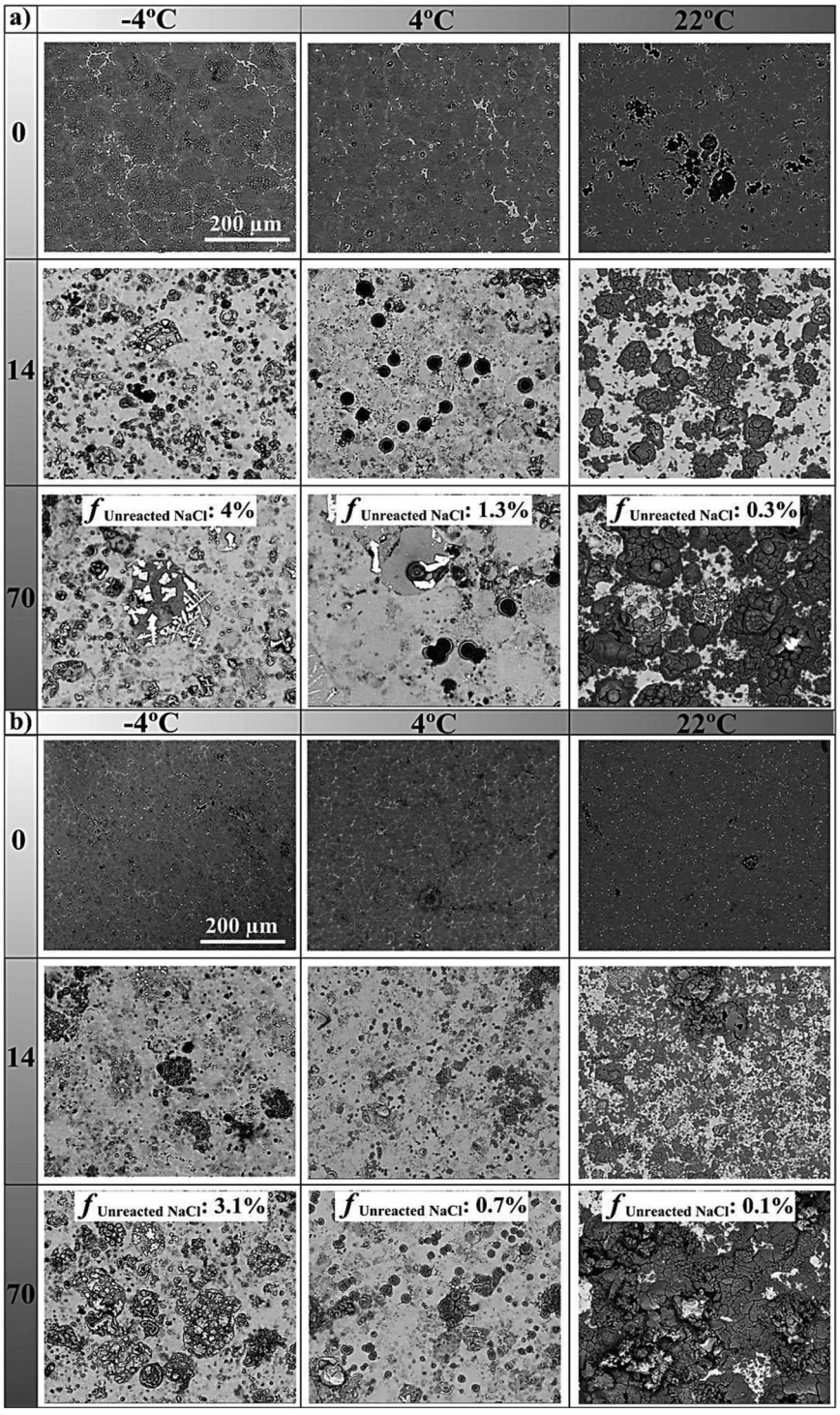

Figure 5. The effect of microstructure, exposure temperature (−4, 4 and 22°C) and NaCl (0, 14, 70 µg/cm^2) on the corrosion morphology after 840 h exposure in the presence of 400 ppm CO_2 and 95% RH; (a) RC AM50, (b) HPDC AM50. The area fraction of the unreacted salt is shown for samples with 70 µg/cm^2 NaCl.

of NaCl are slightly higher for the RC samples than for HPDC AM50. This may signify that RC AM50 corrodes somewhat faster in the very early stages of corrosion. However, further investigations including short-term exposures in the presence of NaCl are required to confirm this statement. In accordance with the results presented above, the lowest mass gain and metal loss values were registered for the RC material at −4°C while the highest mass gain and metal loss values were recorded for the HPDC material at 22°C.

Corrosion products morphology- SEM imaging.—Figure 5 and 6 display plan-view SEM micrographs of corroded surfaces of RC and HPDC samples exposed in different atmospheric environments. The observations confirmed the strong positive correlation between the alloy microstructure and exposure temperature and the rate of atmospheric corrosion found by gravimetry.

The influence of CO_2 and NaCl.—Although major morphological inspections were conducted on alloys exposed in the presence of CO_2, we did also performed SEM imaging on alloys exposed in the absence of CO_2. Irrespective of microstructure and temperature, the corrosion product morphology strongly depended on whether CO_2 was present or not, compare Figs. 5 and 6. In the presence of CO_2, the general morphology of corrosion products was uniform with conspicuous circular features that reflect the location of the NaCl (aq) droplets formed upon exposure to the humid exposure conditions. In contrast, in the absence of CO_2, corrosion is highly localized. Also, the typical length

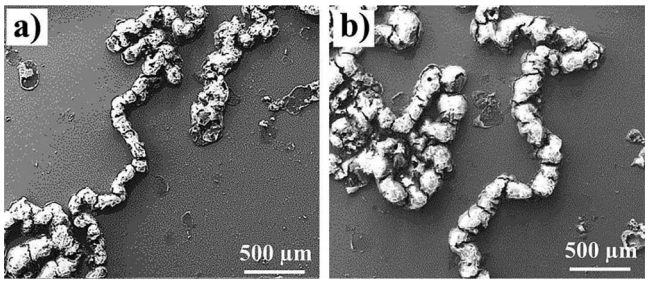

Figure 6. Corrosion product morphology, 70 µg/cm^2 NaCl in the absence of CO_2; (a) RC AM50 at −4°C, (b) HPDC AM50 at −4°C.

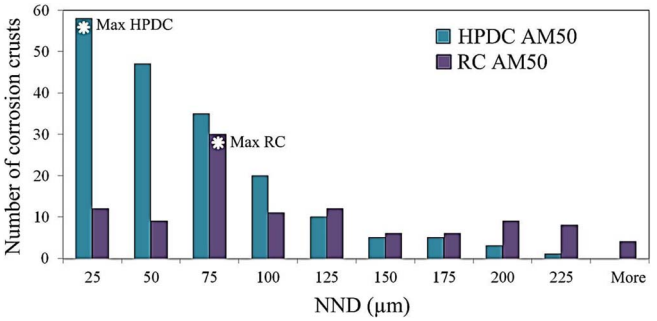

Figure 7. The nearest neighbor distance (NND) and number density of corrosion crusts in the RC and HPDC materials. The total number of corrosion crusts for HPDC and RC materials were 185 and 107, respectively, in an area of 1.5 mm^2. (70 µg/cm^2 NaCl, 400 ppm CO_2, 22°C, 840 h).

scale of corrosion attack depends on the presence of CO_2. Thus, in the absence of CO_2 corrosion products form elongated crusts of 4–7 mm size while in the presence of CO_2 the corrosion products form small circular features of about <200 µm diameter.

The scarce corrosion products observed in the absence of salt are mainly associated with the α-Mg grains, the inter-dendritic region remaining more or less intact. In accordance with the gravimetric data in Fig. 4 and Table IV, the extent of corrosion attack increased with the amount of NaCl added. After 840 h exposure in the presence of 400 ppm of CO_2 and with 70 µg/cm^2 of added NaCl, small amounts of unreacted NaCl crystallites were detected on the corroded surface. They correspond to NaCl (aq) solution present at the end of the exposure that has crystallized upon drying.

The amount of unreacted salt was consistently smaller for HPDC AM50 than for RC AM50. Thus, after corrosion at 22°C the area fraction of NaCl (f_s) was 0.1 and 0.3% for HPDC and RC AM50, respectively. The lower f_s value in the case of HPDC AM50 indicates that a larger fraction of salt has been consumed in the formation of corrosion products. This is in accordance with the gravimetric results (Table IV and Fig. 4) that show faster corrosion of the HPDC material.

The influence of temperature.—The effect of exposure temperature on the corrosion product morphology can be seen in Fig. 5. Increasing the temperature from −4 to 22°C resulted in significantly more corrosion products of both materials, in agreement with the gravimetric results. This trend is also seen in the f_s values, which showed that the fraction of the surface covered by unreacted salt was largest at −4°C.

The influence of microstructure.—The as-cast microstructure largely affected the formation and distribution of corrosion products, see Fig. 5. Quantitative analyses were conducted on RC and HPDC samples exposed at 4°C and NaCl, Fig. 7. There are two crucial findings in Fig. 7. Firstly, the total number of the corrosion crusts in the HPDC material, 185, was significantly higher than the RC material, 107. Secondly, the NND results showed the presence of a large number of corrosion crusts in the low distance intervals (25–75 µm) with a maximum number at the distance of 25 µm for HPDC material. A relatively small number of crusts are formed with the high distance intervals (more than 200 µm). For the RC AM50, the crusts were not as close together as they were in the HPDC material with the maximum number at the distance of 75 µm.

Analyzing the surface damage after corrosion product removal.—Figure 8 shows typical topographical images of the pickled (after corrosion product removal) RC and HPDC materials exposed at 4°C. Such study provided an opportunity to examine the extent of the damage on the surface of the alloys tested. The 3D images clearly show that some regions were corroded away from the alloy surfaces. In accordance with the gravimetric data and morphological examination, the fraction of the corroded areas in the HPDC material was higher than RC material both in the absence and in the presence of 400 ppm CO_2.

Quantitative analyses revealed that the area fraction of pits deeper than 2 µm was about 2.5 times higher in the HPDC material compared the RC material for the case of samples exposed in the presence of CO_2, Besides, the images show that the corrosion pits were bigger

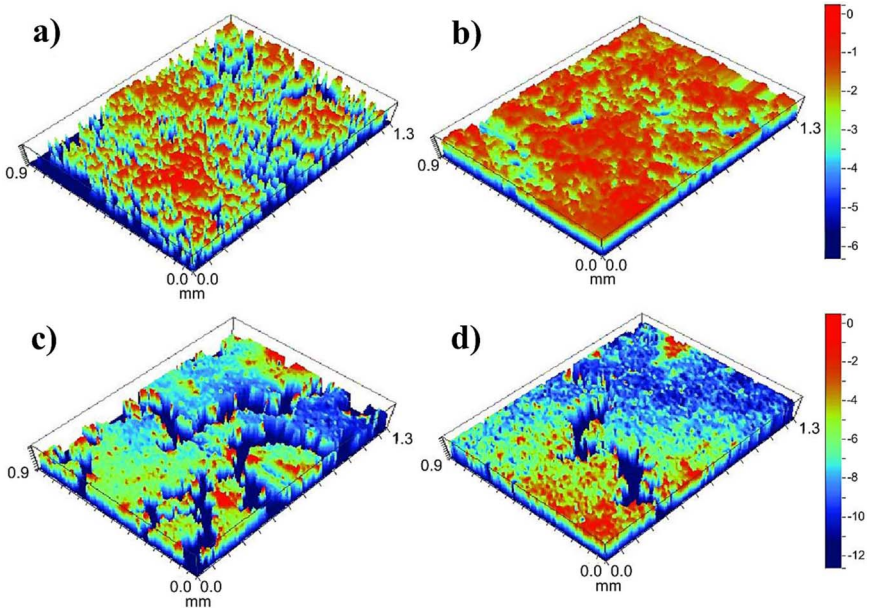

Figure 8. 3D interference topographical images after removal of the corrosion products. Exposures in the presence of ambient level of CO_2 at 4°C; (a) HPDC AM50, (b) RC AM50. Exposures in the absence of CO_2 at 4°C; (c) HPDC AM50, (d) RC AM50. (70 µg/cm^2 NaCl, 400 ppm CO_2, 840 h).

in the case of the RC than HPDC alloy in the samples exposed in the presence of CO_2, which seems to be connected to the size of the α-Mg grains as well as the distribution of the intermetallic particles. The more localized corrosion attack was also evident in the CO_2-free exposure, Figs. 8c and 8d, which agreed well with plan-view SEM images, shown in Fig. 6.

Discussion

The influence of environmental variables.— General corrosion of Mg in the presence of salt.— The NaCl deposited before the experiment absorbs water vapor when the samples are introduced into the corrosion chamber to form a solution that contains about 8% NaCl by weight (at 95% RH).[36] Hence, the corrosion process occurs in the presence of liquid water. When immersed in an aqueous solution containing NaCl, Mg and its alloys are reported to corrode according two electrochemical half reactions. In the first step Mg^{2+} is produced by the anodic dissolution of Mg (2). These ions can combine with OH^- in the electrolyte to precipitate Mg hydroxide (brucite) created by the cathodic reduction of water (3) occurring on different parts of the surface.[2,37,38]

$$Mg(s) \rightarrow Mg^{2+}(aq) + 2e^- \quad [2]$$

$$2\,H_2O + 2e^- \rightarrow H_2(g) + 2\,OH^-(aq) \quad [3]$$

$$Mg^{2+}(aq) + 2OH^-(aq) \rightarrow Mg(OH)_2(s) \quad [4]$$

Mg dissolution results in the accumulation of Cl^- (aq) at the anodic sites, which has been reported to enhance the dissolution of Mg in neutral solution.[15,39] The dominant corrosion product in NaCl (aq) is reported to be brucite according to a chemical reaction 4 that is likely to accumulate in the vicinity of the anodic sites.[29] In the cathodic areas, hydroxide is produced and Na^+ (aq) ions are accumulated, resulting in high pH values, stabilizing the $Mg(OH)_2$ passive film. In an aqueous solution Mg may react according to the reaction 5 resulting in the formation of hydrogen gas and Mg hydroxide. The reaction 5 is the overall reaction with reactions 2–4;[38]

$$Mg(s) + 2H_2O(aq) \rightarrow Mg(OH)_2(s) + H_2(g) \quad [5]$$

While the atmospheric corrosion of Mg alloys in the presence of NaCl at RH = 95% is expected to proceed in a similar way, there are significant differences in comparison to corrosion during immersion because of the small amount of aqueous solution available and the absence of large scale convection.[15] According to Jönsson et al.,[40,41] who investigated the NaCl-induced atmospheric corrosion of Mg-Al alloys, micro-galvanic elements are established where the anodic dissolution mainly occurs in the middle of the primary α-dendrite grains and the cathodic process mainly occurs on the intermetallic phases, i.e. β and η particles.

The results show that the corrosion rate increases with increasing the NaCl concentration. This reflects the well-known corrosivity of NaCl toward Mg and Mg alloys under humid conditions. An increase in the amount of NaCl results in a larger amount of surface electrolyte and an increased surface conductivity in humid environment. This leads to a better micro-galvanic coupling between the α-Mg grains and intermetallic particles.

The effect of CO_2 and temperature.—In order to understand the atmospheric corrosion behavior of Mg alloys in cases where there is a limited supply of CO_2 e.g., in crevices and in occluded areas such as lap joints and beneath coatings, it is useful to consider the effect of CO_2 on corrosion. In this study the RC alloy exhibits consistently better corrosion resistance than the HPDC material in all environments examined (in the absence and presence of CO_2 and at all the three temperatures). However, both alloys exhibited similar trends in the corrosion rates in the different environments. Recently, the authors studied the effect of CO_2 on the atmospheric corrosion of Mg-Al alloy produced by conventional HPDC casting.[35] The presence of 400 ppm of CO_2 (approximately the CO_2 concentration in the ambient atmosphere) was found to inhibit the corrosion of the alloys produced by both casting techniques. CO_2 dissolves in the surface electrolyte where it reacts with the alkali formed in the cathodic reaction;

$$H_2CO_3 + OH^- \rightarrow HCO_3^- \quad [6]$$

$$HCO_3^- + OH^- \rightarrow CO_3^{2-} + H_2O \quad [7]$$

The resulting pH decrease in the electrolyte layer diminishes the solubility of alumina present in the passive film.[35] While the decreased pH increases the solubility of brucite, the Mg hydroxy carbonates formed in the presence of CO_2 are less soluble than brucite and have been suggested to slow down corrosion by blocking anodic and cathodic sites.[29] In accordance with the literature reports, the present SEM observations shows that the presence of 400 ppm CO_2 has a strong effect on corrosion morphology at all temperatures studied (compare Figs. 5 and 6). Thus, in the presence of 400 ppm CO_2, corrosion is initially confined to the NaCl (aq) droplets, while in the absence of CO_2 corrosion is not related to the initial droplet distribution.

The effect of exposure temperature on the corrosion of the Mg alloy AM50 is the subject of our recent paper.[29] The present results show a strong positive temperature dependency for the corrosion of alloys tested, especially in the presence of CO_2 (see Table IV), implying that there is a rate-determining step in the corrosion process of the alloy AM50, which is thermally activated, showing an Arrhenius-type behavior. In the case of 99.97% Mg, the effect of temperature is more complex (See Fig. 4). The atmospheric corrosion is more severe at 4°C. It is suggested that the peculiar temperature dependency of the corrosion rate of 99.97% Mg in the presence of CO_2 is due to competing effects. Thus, the decreasing solubility of CO_2 in water with increasing temperature is expected to slow down carbonatiztion at higher temperature. Conversely, the hydration of CO_2 to form carbonic acid is;

$$CO_2(aq) + H_2O \rightarrow H_2CO_3(aq) \quad [8]$$

This is a relatively slow, activated process that becomes faster at high temperature, promoting carbonatization. The absence of a clear temperature dependency of the corrosion of Mg together with the strong positive temperature effect reported for NaCl-induced atmospheric corrosion of Al[42] suggests that the slowing of the corrosion of alloy AM50 at low temperature is related to the aluminum content in the alloy. Thus, it is suggested that the observed temperature dependency of the atmospheric corrosion of alloy AM50 is related to slower dissolution of alumina in the passive film at low temperature. The current results show that the response to the exposure temperature is the same for the alloys exhibiting different microstructures produced by different casting technologies.

The influence of as-cast microstructure.—The microstructure of the RC AM50 vs. HPDC AM50.— Due to the inherently rapid melt cooling in HPDC and RC, the solidification process is far from equilibrium and can be described by the Scheil equation.[43] Thus, it is well known that β-phase forms during solidification of HPDC Mg-Al alloys at Al contents >2%, even though the solid solubility of Al in the α-Mg phase is about 13% at the eutectic temperature. Also, during subsequent cooling in the solid state, the solubility of Al in the α-Mg phase decreases to about 1% at ambient temperature. Hence there is a driving force for precipitation of β-phase in the solid state.

This is observed in sand mould casting, where cooling rates are slow. In contrast solid state precipitation of β does not seem to take place to any significant extent in RC or HPDC cast AM50, presumably because of the slow diffusion of Al and the fast cooling in the metallic molds. According to the Mg-Al equilibrium phase diagram, solidification of alloy AM50 with about 5% Al starts by the formation of primary α-Mg with an Al-content of about 2%. Due to the slow diffusion of Al in the solid, subsequent grain growth produces cored α-Mg grains with the highest Al content in the periphery. Thus, in the HPDC method, α-Mg dendrites containing a low amount of Al are the first solid particles formed during cooling. The microstructure is

affected by the cooling rate and the dendritic growth can be suppressed by increasing the cooling rate. In contrast, in the case of RC AM50, the stirring of the semi-solid slurry causes the α-Mg grains to become rounded.

The microstructural characteristics depend on bar thicknesses due to different cooling rates. Hence, to compare the microstructure of the alloy produced by the two casting methods, the evaluated areas were obtained from bars of the same thickness and at the same distance from the surface of the casting. As expected, the RC and HPDC materials exhibit major microstructural differences, the differences concerning the β-phase being especially notable. Firstly, the fraction of β phase is much higher in the RC material than in HPDC material, which is very likely related to the cooling rate as well as the less dendritic structure of α-Mg grains in the RC process, as described in.[31] Besides, the higher fraction of inter-dendritic regions (about 2 times higher compared to the RC material) in the HPDC alloy could explain the lower conductivity of the β phase particles in the HPDC material. Another major difference is that the β phase exhibits a high degree of connectivity (i.e., forming relatively large elongated particles) in the RC material while it forms smaller and more dispersed particles in the HPDC alloy (See Fig. 2b and 2d).

Another important difference between the two materials is that the distribution of β phase is macroscopically highly non-uniform in the HPDC material, as shown in Figs. 2a and 2b. Therefore, HPDC AM50 exhibits regions with a strong accumulation of β phase (Fig. 3a), while other regions are poor in β phase (see Fig. 3b). This undesirable agglomeration tendency of the HPDC material may also influence the measured area fraction of β phase particles in the investigated regions.

The presence of larger and network-like β phase in RC material can be explained by considering the special type of solidification that takes place during semi-solid casting. The slurry preparation process in RC technique consists of nucleation of α-Mg grains and their non-dendritic growth. The growth process occurs during the slow and controlled cooling from the melting temperature for the formation of the semi-solid. During the secondary solidification in the die cavity, all the eutectic is concentrated in the liquid regions between the primary α-Mg grains. A consequence of the non-dendritic morphology is that the specific solid-liquid interfacial area is smaller, meaning that the β phase growth will be less restricted than in the case of HPDC material. Hence, the β phase forms large continuous particles rather than fine and disperse particles as in HPDC material.

The quantitative measurements reveal that the primary α-Mg grains are larger and have higher aspect ratios in the RC material compared to the HPDC material, see Table III. The formation of large primary α-Mg in the microstructure of RC material is attributed to the presence of large pre-formed grains during solidification in die cavity.[45,46] Besides, the dendritic structure is less pronounced in the microstructure of RC alloy than in the HPDC material as result of the secondary solidification in the die cavity as well as higher amount of shear during the filling process.[44,45] In a parallel study it was shown that there is a tendency for α-Mg grains to move away from the surface during cavity filling thereby causing a higher overall Al-content in the surface regions.[46] This is a known phenomenon for semi solid slurries as are used in the RC method. In the case of HPDC, some solidification often takes place in the shot sleeve. These grains, referred to as externally solidified grains (ESG's), tend to get fragmented during the passage of the melt through the gating system. Such macro-segregation, and the related Al concentration profile over a cross section, will of course have an impact on the corrosion behavior. The concentration of Al in the center of the primary α-Mg grains is found to be somewhat higher in the HPDC material. The reasons behind this difference will be the subject of further investigation.

We have examined an alloy AM50 that was produced by the RC technique, in which the slurry was prepared using the newly developed RheoMetal process. In the RheoMetal process, melt cooling is achieved by using an enthalpy exchange material (EEM) attached to a stirrer. In this way the melt is internally cooled, eliminating the need for external heat flow control, and creating a robust process where large amounts of high quality slurry can be produced in a short time. In the present study the slurry is cast in a specially designed squeeze casting machine that features a vertical shot sleeve where the degree of filling is 100%, reducing heat losses before the slurry is injected into the casting tool. In a traditional horizontal high pressure die casting machine the degree of filling in the shot sleeve is typically 30–40%. Due to the low heat content of the semi-solid Mg slurry, it is of utmost importance to minimize heat losses. The corrosion resistance of the alloy produced by the RheoMetal process is significantly better than HPDC AM50. This is demonstrated by mass gain and metal loss data, in good agreement with top-view SEM micrographs of corroded samples. To explore the underlying reason behind this difference it is essential to be aware of the role of different constituents on the corrosion behavior of Mg-Al alloys.

The effect of microstructural constituents.—Because the global chemical compositions of the two materials are the same, the different corrosion behavior must be due to differences in microstructure. However, explaining the differences in corrosion behavior of the RC material and the HPDC alloys is rather complicated as there are contradictions between our results and those presented in the literature. Perhaps the starkest contrast between literature and the presented results is the role of α-Mg grains size on the corrosion of Mg alloy AM50. The introduction mentions the well-known dual effect of β phase particles on the corrosion behavior of Mg-Al alloys. Considering that the β phase is continuous and encapsulates the α-grains, it is argued that the selective corrosion of α-Mg would result in the formation of a relatively corrosion resistant β-phase surface layer. In this scenario the connectivity of the β phase becomes critical for corrosion properties. Song et al.[47] argues that alloys exhibiting large α-Mg grains tend to corrode faster because the α phase is not protected by the β phase, or by the corrosion products, the β phase acting as cathodic sites. Conversely, they argue that if the α-Mg grains are small, the β phase is almost continuously distributed along the inter-dendritic regions, making it possible for the β phase to act as a corrosion barrier. This means that the present results are apparently at odds with this view and suggest a different interpretation of the effect of microstructural configuration on the corrosion of Mg alloys. Thus, the RC material, which is better from the corrosion point of view, exhibits larger α-Mg grains compared to the HPDC material. While considering the effect of grain size on the corrosion of Mg-Al alloys, these results are also in contradiction with the results presented in the literature since there are studies proving that Mg-Al alloys with fine grained structure are more favorable than coarse grained alloys from the corrosion point of view.[17,48–50]

Mathieu et al.[51] suggested that the slower corrosion of semi-solid cast AZ 91 compared to the same alloy in HPDC form is explained by a higher Al content in the α-phase, the rate of galvanic corrosion between α and β phases decreasing with increasing the Al content in α phase. However, the present results are not in agreement with this suggestion either as the EDX analyses show that the Al content of the α-phase is almost the same in alloy AM50 produced by RC and HPDC techniques. This is especially the case if scatters of the EDX analyses of the Al content in α-Mg grains of HPDC and RC material, presented in the results part, are taken into accounts. We considered the detailed microstructural arrangement of the constituents in "statistical manner" to elucidate the reason(s) behind the difference in the corrosion behavior of the alloys. When comparing the corrosion behavior of HPDC and RC AM50, it seems that the different corrosion resistance of the two materials seems to be related to the area fraction, size, morphology and distribution of intermetallic phase particles and not to the size or Al content of the α-Mg grains. This line of reasoning is pursued below.

The results showed that, although the RC material exhibits larger α-Mg grains, micro-galvanic corrosion appears not to be intensified. As mentioned earlier, this can be attributed to the higher fraction of β phase with more continuous and network-like morphology in the RC material. However, it should be considered that the micro-galvanic corrosion process could be more intensified in the initial stages of corrosion of the RC alloy due to the higher proportion of β-phase, but, the β -phase network could later slow down this process. The statistical

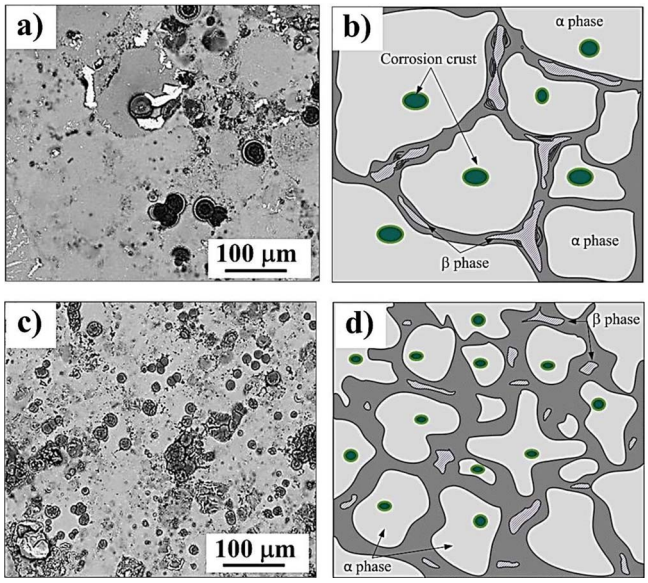

Figure 9. SEM image and schematic illustration of the corroded samples exposed at 4°C and 70 µg/cm^2 NaCl, (a) the RC AM50, (b) schematic of the microstructure and distribution of corrosion crusts in the RC AM50, (c) the HPDC AM50, (d) schematic of the microstructure and distribution of corrosion crusts in the HPDC AM50.

analyses, presented in Fig. 3, outline an alternative explanation. The as-cast microstructure of HPDC material exhibits finer and larger number of intermetallic particles. It is argued that the faster corrosion of HPDC AM50 is partially due to the formation of a larger number of micro-cells compared to the RC AM50. In addition to the plan-view SEM images, the 3D images of the corroded surfaces in Figs. 8a and 8b also support this statement. This hypothesis is also substituted by the quantitative work done on the corroded samples, which indicated that the number density of corrosion products is much higher in the HPDC AM50 than RC AM50, see Fig. 7. This is in agreement with the distribution of corrosion products on the sample surface; compare the plan-view SEM images in Fig. 5a with those of Fig. 5b. These results show that the corrosion of Mg-Al alloys is under cathodic control, not anodic control, and that the β phase is the main locus of the cathodic reaction on Mg-Al alloys.

The NND results showed that the corrosion products are much closer in the case of the HPDC AM50 compared to RC AM50. The size of the α-Mg gains, which are larger in the RC alloy than the HPDC alloy, could explain the NND results. This provides additional explanation for the considerably better corrosion resistance of the RC alloy; lower density of α-Mg grains in the RC material in an area of similar size than the HPDC material could also play a role in the better corrosion resistance of the RC AM50. Figure 9 shows two representative SEM images of the corroded RC and HPDC samples and the corresponding schematic showing the effect of microstructural configuration on the formation corrosion products in the two alloys. The discussion provided above can be comprehended from the schematic illustration in Fig. 9. As seen, larger α-Mg grains as well as fewer β phase particles resulted to the formation of less corrosion cells/crusts and as a result much better corrosion behavior in the RC AM50 than HPDC AM50. Although the barrier effect of the β phase was not proven in this study due to the rather short-term exposures, it is expected that this effect becomes much more pronounced in the RC AM50 than HPDC AM50 in more corrosive environments/longer exposure times, similar to the observations made by Pardo et al.[52]

The statistical data showed that the area fraction of η particles was considerably less than that of the β phase particles; compare the data presented in Table III with the area fraction of η particles. This would reflect the crucial role of the of β phase in the corrosion of the alloy AM50. However, as mentioned earlier, the η phase particles also act as cathode in the microstructure of Mg-Al alloys. The slightly less fraction of η particles in the RC material (0.35%) than the HPDC alloy (0.4%) can be another reason for the better corrosion resistance of the RC AM50. The role of casting technology on the area fraction of intermetallic phase particles is discussed elsewhere.[31]

From mechanical properties point of view, while considering the α-Mg grain size and intermetallic characteristics, requirements are contradictory. For instance, fine grains are beneficial for fatigue, but coarse grain enhances creep resistance, see Refs. 53 and 54. This kind of microstructural configuration (as in the RC AM50) may not be desired for application where tensile properties are of importance. On the other hand, the strong agglomeration of brittle intermetallic particles observed in the HPDC material (see Fig. 3) is expected to have a harmful effect on the yield strength of the cast alloys. Thus, predicting the mechanical properties of the RC alloy can be quite difficult and further investigations are required to understand the effect of RheoMetal process on the mechanical properties of Mg-Al alloys.

We showed that density of macro- and micro-porosities is higher in HPDC AM50, see Table III. The formation and distribution of porosity is reported to be influenced by processing variables such as gate velocity and melt temperature.[55] Thus, it is suggested that the lower porosity in the RC material is due to a high shearing of the semi-solid slurry during rheocasting. Also, the tendency for trapping air during cavity filling is smaller in the RC process because of the laminar flow of the melt. Further, since the semi-solid slurry contains a large content of solid phase (typically around 30–40%), the solidification shrinkage will be smaller.[31] Although the deteriorating influence of porosity on the mechanical properties of the Mg alloys is well-known, the effect of porosity on the atmospheric corrosion behavior of Mg-Al alloys is not known. Thus, further research on the relationship between casting porosity and the corrosion of Mg-Al alloys is warranted.

Conclusions

The corrosion behavior of RC AM50 and HPDC AM50 was investigated at three different temperatures. The results of this study demonstrated that it is possible to greatly improve the corrosion resistance of Mg-Al alloys by changing the microstructural configurations. The observations made in this study are as follows;

- The corrosion of alloy AM50 depends on casting technology, the rheocast material showing better corrosion behavior than AM50 in the HPDC state. The advantage of the RC material in this respect is especially evident in the presence of CO_2 and at low temperature.
- The improved corrosion resistance of RC AM50 is attributed to the differences in the microstructure of the alloy produced by the two routes:
  - The microstructure of RC AM50 exhibits larger primary α-Mg grains having a higher aspect ratio compared to HPDC AM50. Also, casting porosity is lower in the RC material by a factor of about 3.
  - While the β phase particles had about 3 times higher area fraction in RC AM50 compared to the HPDC material, the β-phase particles exhibited a smaller number density and were more continuous and network-like. The higher β phase fraction in the RC material is primarily attributed to the RC material exhibiting a lower fraction of inter-dendritic material with a correspondingly higher Al content as well as no tendency for agglomeration of β phase particles.
  - The larger number of cathodic sites that are well dispersed leads to the formation of a larger number of micro-cells for the HPDC material. In other words, there is a direct relation between the number density of intermetallic particles and corrosion products. Also, the of β phase "barrier effect" is expected to be present in the RC material and not for HPDC AM50 because of the more network-like morphology of β phase, and as a result a better surface coverage, in the former case.

• Lowering the temperature from 22 to 4 and −4°C decreases the corrosion rate significantly for both RC and HPDC AM50. Also, ambient concentrations of CO_2 inhibit the NaCl-induced corrosion of both materials.

References

1. M. M. Advedesian and H. Baker, *Magnesium and magnesium alloys*, *ASM Specialty Handbook*, ASM International, Materials Park (1999).
2. G. L. Song and A. Atrens, *Adv. Eng. Mater.*, **1**, 11 (1999).
3. Z. M. Shi, G. L. Song, and A. Atrens, *Corros. Sci.*, **48**, 1939 (2006).
4. P. B. Srinivasan, C. Blawert, W. Dietzet, and K. U. Kainer, *Scrip. Mater.*, **59**, 43 (2008).
5. G. Song and A. Atrens, *Adv. Eng. Mater.*, **5**, 837 (2003).
6. J. E. Gray and B. Luan, *J. Alloys Comp.*, **336**, 88 (2002).
7. G. L. Makar and J. Kruger, *Int. Mater. Rev.*, **38**, 138 (1993).
8. Y. K. Kim, S. W. Sohn, D. H. Kim, W. T. Kim, and D. H. Kim, *J. Alloys Compd.*, **549**, 46 (2013).
9. E. F. Emley, *Principals of magnesium technology*, Pergamon Press, Oxford (1966).
10. M. Siedersleben, *Vakuum-Druckguss von Magnesiumlegierungen fur hochbelastete Bauteile, Magnesium Eigenschaften*, Wiley-VCH, Weinheim (2000).
11. Z. Fan, *Int. Mater. Rev.*, **47**, 49 (2002).
12. Z. Koren, H. Rosenson, E. M. Gutman, Y. B. Unigovski, and A. Eliezer, *J. Light. Met.*, **2**, 81 (2002).
13. H. Cao and M. Wessén, International patent application No. PCT/SE2005/001889.
14. H. P. Godard, W. B. Jepson, M. R. Bothwell, and R. L. Lane, *The corrosion of light metals*, Wiley and Sons, New York (1967).
15. G. L. Song, *Adv. Eng. Mater.*, **7**, 563 (2005).
16. R. M. Asmussen, P. Jakupia, M. Danaie, G. A. Botton, and D. W. Shoesmith, *Corros. Sci.*,**75**, 114 (2013).
17. R. M. Asmussen, W. J. Binns, P. Jakupi, and D. W. Shoesmith, *J. Electrochem. Soc.*, **161**, C501 (2014).
18. M. Danaie, R. M. Asmussen, P. Jakupia, D. W. Shoesmith, and G. A. Botton, *Corros. Sci.*, **77**, 151 (2013).
19. H. Y. Ha, J. Y. Kang, C. D. Yim, J. Yang, and B. S. You, *Corros. Sci.* **89**, 275 (2014).
20. X. Y. Sun, B. Zhang, H. Q. Lin, Y. Zhou, L. Sun, J. Q. Wang, E.-H. Han, and W. Ke, *Corros. Sci.*, **77**, 103 (2013).
21. M. Jönsson, D. Persson, and R. Gubner, *J. Electrochem. Soc.*, **154**, C684 (2007).
22. M. Jönsson, D. Persson, and D. Thierry, *Corros. Sci.* **49**, 1540 (2007).
23. R. Lindström, J. E. Svensson, and L. G. Johansson, *J. Electrochem. Soc.* **149**, B103 (2002).
24. G. L. Song, A. Atrens, D. StJhon, J. Nairn, and Y. Li, *Corros. Sci.*, **39**, 855 (1997).
25. Y. Song, E. H. Han, K. Dong, D. Shan, C. D. Yim, and B. S. Corros. *Sci.*, **88**, 215 (2014).
26. O. Lunder, J. E. Lein, T. Kr Aune, and K. Nisancioglu, *Corrosion*, **45**, 741 (1989).
27. M. Danaie, R. M. Asmussen, P. Jakupia, D. W. Shoesmith, and G. A. Botton, *Corros. Sci.*, **83**, 299 (2014).
28. R. Ambat, N. N. Aung, and W. Zhou, *Corros. Sci.*, **42**, 1433 (2000).
29. M. Esmaily, M. Shahabi-Navid, J. E. Svensson, M. Halvarsson, L. Nyborg, Y. Cao, and L. G. Johansson, *Corros. Sci.*, **90**, 420 (2014).
30. J. Chen, J. Q. Wang, E. H. Han, and W. Ke, *Corr. Eng., Sci. Tech.*, **46**, 277 (2011).
31. M. Esmaily, M. Shahabi-Navid, N. Mortazavi, J. E. Svensson, M. Halvarsson, M. Wessén, A. E. W. Jarfors, and L. G. Johansson, *Mater. Charac.*, **95**, 50 (2014).
32. J. Balej, *Int. J. Hydro. Ener.*, **10**, 233 (1985).
33. D. G. Prakash, D. Regener, and W. J. J. Vorster, *Comp. Mater. Sci.*, **43**, 759 (2008).
34. A. Tewari and A. M. Gokhale, *Acta Mater.*, **54**, 1957 (2006).
35. M. Shahabi-Navid, M. Esmaily, J. E. Svensson, M. Halvarsson, L. Nyborg, Y. Cao, and L. G. Johansson, *J. Electrochem. Soc.*, **161**, C277 (2014).
36. M. J. Blandamer, J. B. F. Engberts, P. T. Glesson, and J. R. Reis, *Chem. Soc. Rev.* **34**, 440 (2005).
37. G. L. Song, A. Atrens, and M. Dargusch, *Corros. Sci.*, **41**, 249 (2002).
38. S. Thomas, N. V. Medhekar, G. S. Frankel, and N. Birbilis, *Curr. Opin. Solid State Mater. Sci.,* In press (2014).
39. Q. Qu, J. Ma, L. Wang, L. Li, W. Bai, and Z. Ding, *Corros. Sci.*, **53**, 1186 (2011).
40. M. Jönsson, D. Thierry, and N. LeBozecb, *Corros. Sci.*, **48**, 1193 (2006).
41. M. Jönsson, D. Persson, and C. Leygraf, *Corros. Sci.*, **50**, 1406 (2008).
42. D. B. Blücher, J. E. Svensson, and L. G. Johansson, *J. Electrochem. Soc.*, **150**, B93 (2003).
43. H.E. Friedrich and B. Mordike, *Magnesium technology*, Springer-Verlag, Berlin (2006).
44. T. J. Chen, X. D. Jiang, Y. Ma, Y. D. Li, and Y. Hao, *J. Alloy. Comp.*, **505**, 476 (2010).
45. S. Ji, M. Qian, and Z. Fan, *Metall. Mater. Trans. A.*, **37**, 779 (2006).
46. M. Östklint, M. Wessén, and A. E. W. Jarfors, *Int. J. Cast Metal. Res.*, **27**, 235 (2014).
47. G. L. Song, A. Atrens, and M. Dargusch, *Corros. Sci.*, **41**, 249 (2002).
48. M. Alvarez-Lopez, M. D. Pereda, J. A. del Valle, M. Fernandez-Lorenzo, M. C. Garcia-Alonso, O. A. Ruano, and M. L. Escudero, *Acta Biomater.*, **6**, 1763 (2010).
49. G. R. Argade, S. K. Panigrahi, and R. S. Mishra, *Corros. Sci.*, **58**, 145 (2012).
50. N. N. Aung and W. Zhou, *Corros. Sci.*, **52**, 589 (2010).
51. S. Mathieu, C. Rapin, J. Steinmetz, and P. Steinmetz, *Corros. Sci.*, **45**, 2741 (2003).
52. A. Pardo, M. C. Merino, A. E. Coy, R. Arrabal, F. Viejo, and E. Matykina, *Corros. Sci.*, **50**, 823 (2008).
53. S. Ji, M. Qian, and Z. Fan, *Metall. Mater. Trans. A*, **37**, 779 (2006).
54. X. Dua and E. Zhang, *Mater. Lett.*, **61**, 2333 (2007).
55. S. G. Lee, A. M. Gokhale, G. R. Patel, and M. Evans, *Mater. Sci. Eng. A*, **427**, 99 (2006).